Preprint Cambridge Centre for Computational Chemical Engineering ISSN 1473 – 4273

Flexoelectricity and the formation of carbon nanoparticles in flames

Jacob W. Martin[1], Maria L. Botero[2], Radomir I. Slavchov[1], Kimberly Bowal[1], Jethro Akroyd[1], Sebastian Mosbach[1] and Markus Kraft[1,3,4]

released: 17 August 2018

[1] Department of Chemical Engineering and Biotechnology
University of Cambridge
West Site
Philippa Fawcett Drive
Cambridge, CB3 0AS
United Kingdom
E-mail: mk306@cam.ac.uk

[2] Department of Mechanical Engineering
National University of Singapore
9 Engineering Drive
Singapore, 117576

[3] School of Chemical and Biomedical Engineering
Nanyang Technological University
62 Nanyang Drive
Singapore, 637459

[4] Cambridge Centre for Advanced Research and Education in Singapore (CARES)
CREATE Tower
1 Create Way
Singapore, 138602

Preprint No. 207

UNIVERSITY OF CAMBRIDGE

Keywords: soot formation, polar aromatics, curved PAH, ion-induced nucleation

Edited by
Computational Modelling Group
Department of Chemical Engineering and Biotechnology
University of Cambridge
West Site, Philippa Fawcett Drive
Cambridge, CB3 0AS
United Kingdom

Fax: + 44 (0)1223 334796
E-Mail: c4e@cam.ac.uk
World Wide Web: http://como.cheng.cam.ac.uk/

Abstract

The formation of carbon nanoparticles in flames involves a nucleation step that remains poorly understood. Experimentally, carbon nuclei formation is known to depend strongly on the electrical aspects of combustion but modes of interaction between charged species in the flame and carbon precursors have yet to be found. We present evidence for flexoelectrically polarised aromatics contributing to carbon nanoparticulate nucleation. We imaged the nascent nanoparticles using high resolution transmission electron microscopy, which revealed that the majority of aromatics in the early carbon nanoparticles are fullerene-like and curved. The curvature induces a significant molecular flexoelectric dipole moment in the polyaromatic hydrocarbons. This electric polarisation allows these molecules to strongly interact with chemi-ions produced during combustion, which we demonstrate using electronic structure calculations. The results indicate that the physical interaction between fullerene-like polar aromatics and chemi-ions is critically assisting the nucleation, and opens a new route to reduce pollution and improve flame-produced nanomaterials.

Highlights

- Curved polycyclic aromatic hydrocarbons are quantified in carbon nanoparticles early in a diffusion flame
- >62.5% are found to contain internal pentagonal rings at 10 mm above the burner.
- The polarity of a curved arenes suggested from the microscopy is 5.32 debye, which is significant.
- Electronic structure calculations reveal strong binding between this polar species and chemi-ions, suggesting a potential nucleation mode.

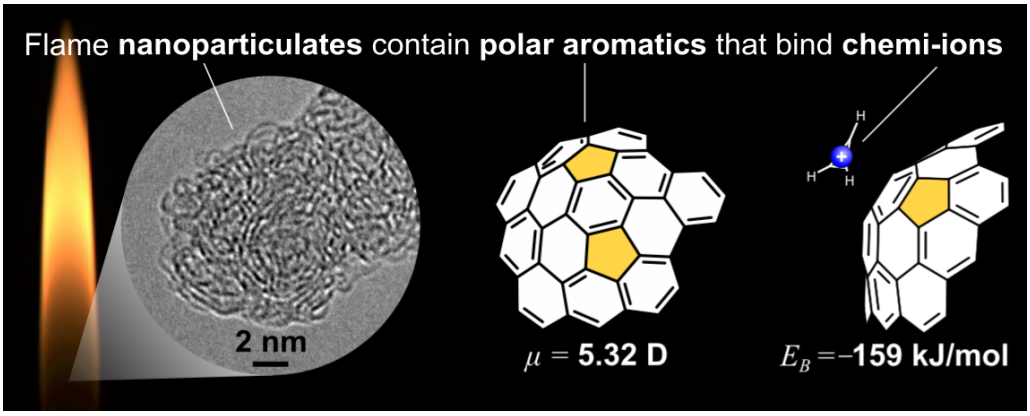

Contents

1 Introduction 3

2 Methodology 5

3 Results and discussion 6

4 Conclusions 10

5 Appendix 11

References 15

1 Introduction

Air pollution from combustion leads to respiratory diseases [23] and contributes to the warming of the planet [31]. Flames can also synthesise a variety of useful carbon particles and nanomaterials for applications in lithium ion batteries, conductive inks and solar cells [37]. The critical step in reducing harmful particulates or controlling the synthesis of useful carbon nanoparticles in flames is the nucleation process where pericondensed polycyclic aromatic molecules (PAHs) form carbon nuclei 1–3 nm in diameter. Yet despite many decades of research on carbon formation during combustion the mechanism of this nucleation process remains elusive [44].

The electrical aspects of carbon nanoparticle nucleation in flames, such as charging processes and the influence of external electric fields, have been studied since the 1950s [9, 24]. Chemical reactions with vibrationally excited carbyne (CH*) readily produce chemi-ions, such as the formyl (CHO^+), cyclopropenyl ($C_3H_3^+$) and hydronium (H_3O^+) cations, at significant concentrations in the flame ($10^{15} - 10^{17}$ m^{-3} [9, 24]). As these ions are consumed in the combustion process, the carbon nuclei form in similar concentrations ($10^{14} - 10^{16}$ m^{-3} [3, 16, 17]). Recently, high resolution particle analysers revealed that up to 95% of the sub-3 nm carbon nuclei are charged [45]. A proportion of these nuclei grow into what are referred to as primary particles (20–30 nm in diameter), eventually coagulating into large, multiply charged fractal aggregates [33].

The many charged molecules and particles in flames can be manipulated using electric fields [34, 38] and a resulting significant reduction or complete eradication of particulates has been demonstrated [30, 34]. Figure 1 shows the impact of an electric field on the flame in a counterflow diffusion ethylene burner. The disappearance of the luminous yellow carbon particulates is clearly visible and has been ascribed to removal of the charged nuclei from the pyrolysis zone by the field [24]. Recent laser induced incandescence and fluorescence imaging of the carbon particulates and molecular species, respectively, in a similar burner configuration, confirmed that the electric field removed the carbon particulates whilst the gas phase chemistry was only minimally changed, suggesting the field primarily influenced the process of nucleation [34].

The concentration of ions in a flame can be artificially increased through the addition of alkali and other metals, which easily ionise at flame temperatures. Electron microscopy [40] and small angle X-ray diffraction [7] revealed that primary particles increased in number and decreased in size with these metal additives, with significant reductions in the mass of particulates produced (50–90% reduction being reported for polystyrene combustion [5]). The role of metal ions in carbon particulate reduction was considered to be due to the ions stabilising nuclei, producing large numbers of smaller carbon particles with increased surface area allowing for their rapid oxidation and destruction [18]. A similar effect was achieved by application of a strong electric field to the flame, drawing positive chemi-ions from the flame zone to the pyrolysis zone [35]. This effect has found application in the design of organometallic anti-smoke additives for diesel [27]. The ability of various metal ions to decrease smoke was found to follow the series Ba > Ca > Ni > Na, K, Zn. According to Magaril and Magaril, Ba and Ca have stronger effects due to their low ionisation energies; the series suggests that the ratio (ionic charge)^2/(ionic radius) is also a factor, which is evidence for nucleation on ions [20].

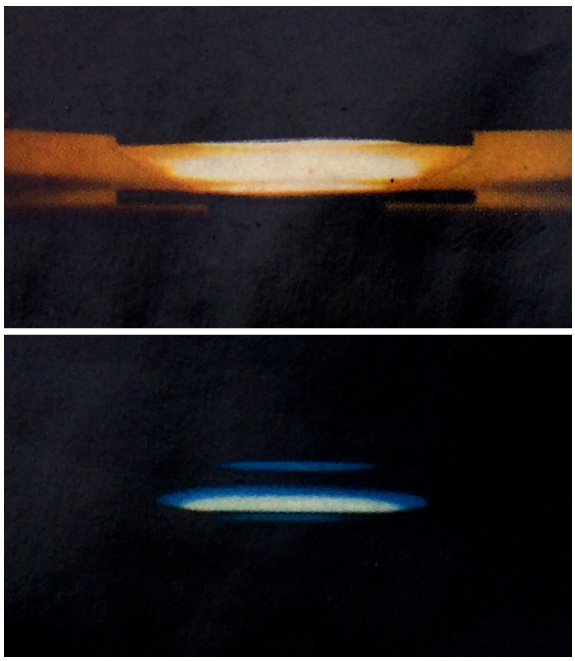

Figure 1: ***Effect of an external normal electric field applied to the flame:*** *counterflow $C_2H_4/O_2/N_2$ diffusion flame without (top) and with (bottom) an electric potential difference of 1 kV applied. Luminous carbon particulates (yellow) disappear from the flame by application of the field (from Lawton and Weinberg [24] 'Electrical aspects of combustion', used with permission from Oxford University Press).*

While the suggestion of ions assisting nucleation is not new, the search for the interaction between ions and the aromatic precursors responsible for the observed effects has been unsuccessful. One suggestion was that the effect is chemical kinetic in nature [3, 35]: Calcote assumed that chemi-ions may promote rapid polymerisation due to ion-induced dipole interactions, forming polycyclic aromatic hydrocarbons (PAHs) and then larger nuclei. However, this mechanism cannot explain the effect of Ba^{2+} and Ca^{2+}. The chemical mechanism for PAH formation was instead found to be due to the radical mechanism (hydrogen abstraction and acetylene addition, HACA); the rate of ion-enhanced polymerisation reactions was found to be too low at flame temperatures [10, 12]. The possibility of heterogeneous nucleation of planar PAHs on ions has also been investigated using electronic structure calculations [4]. The electrostatic interaction between a chemi-ion and planar PAHs was found to result in binding of the ion around the rim of the planar PAH; however, energies were insufficient to stabilise the ion-PAH complexes at temperatures at which carbon nanoparticles forms in the flame 1300–1500 K [14].

What interaction is then holding the PAH molecules and the charge together in a nucleus? Recent electron microscopy of carbon particulates has demonstrated that they contain a significant number of non-planar PAH molecules [1, 43]. Furthermore, curved aromatics such as corannulene have been extracted from carbon particulates [22, 47], and even completely closed carbon cages (e.g., C_{60} and C_{70} fullerenes) have been synthesised in low-pressure benzene flames [13, 36]. PAHs can curve through the integration of non-

hexagonal rings into their structure that become completely surrounded by hexagonal rings. The process has been predicted to occur through the HACA mechanism of acetylene addition to an armchair functional site possessing a pentagonal ring [11]:

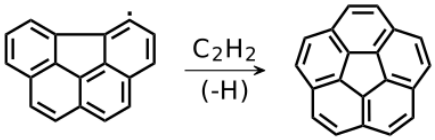

Despite curved PAHs being less energetically favoured compared with planar PAH kinetic analysis suggested that the pentagonal ring enclosure does occur at flame conditions, albeit at a slower rate compared to hexagonal ring integration [46, 48]. This mechanism suggests that the precursors of the curved molecules are smaller PAHs containing five-membered rings, which are well-known to be among the most abundant PAHs in the flame (as much as 25% of those smaller than C_{24} [9]).

Something peculiar about curved PAHs is that they are highly polar molecules. We recently performed electronic structure calculations on large curved aromatic molecules [28] and found a significant flexoelectric dipole moment for curved PAHs (4–6.5 D – approximately two to three times that of water at 1.85 D [39]). Many small flat PAHs containing pentagons are also polar [29]. In addition, the dispersion and ion-induced dipole interactions between an ion and a curved PAH are significantly higher for an ion attached at the concave side of the curved PAH compared to ion-planar PAHs (due to closer contact). Thus, the interaction between polar PAHs and ions is stronger and much more long-ranged than the planar PAH-ion, which has applications including the use of curved PAHs to store large amounts of lithium in battery anodes [49].

In this work, we present evidence of large amounts of polar aromatics in the nascent carbon nanoparticles and calculate significant binding energies between a representative polar PAH with the cation $C_3H_3^+$.

2 Methodology

Carbon particulates were sampled thermophoretically from an ethylene coflow diffusion flame using a rapid solenoid injector and imaged with an electron microscope (Figure 2a and b), where fringes (elongated dark regions where the electron beam intensity was reduced) in the high resolution transmission electron microscopy (HRTEM) micrograph correspond to imaging across the plane of an aromatic molecule (see Figure 2c and d).

We analysed these fringes using custom image-analysis software which skeletonises the fringes into discrete lines for which geometrical parameters were calculated: length (L), end-to-end distance (C), and tortuosity ($\tau = L/C$). We have previously benchmarked the accuracy of the fringe analysis against simulated HRTEM images of planar PAHs [1]. Our software was modified to analyse the fringes of 209 primary particles, as a function of the radius from the centre of the particle and the sampling height above the burner. The earliest carbon nanoparticulates that could be sampled were at 10 mm above the burner. These early particles, $\sim$10 nm in diameter, provide insight into the aromatic content in

the carbon nuclei, which cannot be directly sampled thermophoretically or imaged due to their small size. Figure 2c and d shows the skeletonised fringes from two representative primary particles – one early particle 10 mm above the burner, where luminosity has yet to develop, and another from the tip (at 49 mm above the burner) – along with the electron micrographs of the particles before image processing. For the radial dependence, fringes were partitioned into five equal-radius concentric spherical shells, and the fringe size and tortuosity distributions were calculated for each shell. The distributions were positively skewed towards longer fringes; therefore, we preferred to use the median length and tortuosity instead of the mean (further details can be found in the Appendix).

3 Results and discussion

The size of the molecular fragments in the nanoparticles can be inferred from the fringe length. Figure 2f shows the fringe lengths across all heights above the burner. The fringes' median size ranges from 0.9–1.2 nm, corresponding to aromatics with 14–22 aromatic rings (assuming a circular pericondensed aromatic [1]). The results for the lowest height above the burner (10 mm) provide insight into the species present at nuclei formation; there, $L = 0.9 - 1.05$ nm, corresponding to a size of 15 aromatic rings, consistent with optical band gap measurements [1] and mass spectrometry [25].

The amount of curved PAHs in the carbon nanoparticles was quantified by analysing the tortuosity of the fringes. The tortuosity is a measure of the curvature, and therefore, of the polarity of the molecular fragments corresponding to a fringe. The majority of fringes in the nanoparticles at 10 mm abover the burner contained a single peak in the curvature and no inflection, indicating the incorporation of pentagons, not heptagons, into the aromatic molecules at this low height (which was also observed by Wang et al. [43]). As seen in Figure 2e, the fringes became less tortuous as the carbon particulates progress through the flame, initially starting at τ =1.18–1.20 and finally leaving the flame with values of τ =1.15–1.17.

The correspondence between the tortuosity and number of pentagons was analysed by simulating HRTEM images of curved PAHs with the similar number of aromatic rings (15) as seen in the early flame, with three, two and one enclosed pentagons (Figure 3a, b and c). The same fringe analysis software was applied to these simulated images and tortuosity values of 1.37, 1.20 and 1.13 were found. Small crosslinked PAHs were also analysed as alternative species that could produce tortuous fringes (see the Appendix Figure S3). The orientation with the maximum fringe tortuosity we could produce for a non-pentagonal PAH crosslinked species was τ =1.15, a value similar to τ of a curved PAH with a single pentagonal ring. We therefore considered fringes with tortuosity values >1.15 to be predominantly due to pentagon integration and not crosslinked species. This cutoff underestimates the amount of curved aromatics due to pentagon integration as it is not possible to distinguish them from crosslinked PAHs. Using this cutoff we calculated that for the lowest sampled height, at least 62.5% of the fringes indicated pentagon integration. This amount of pentagon integration is higher than the values 28–49% found previously for mature carbon particulates [43, 48]. These lower values can be explained by the age of the particles; indeed, the fringe analysis for carbon particulates sampled

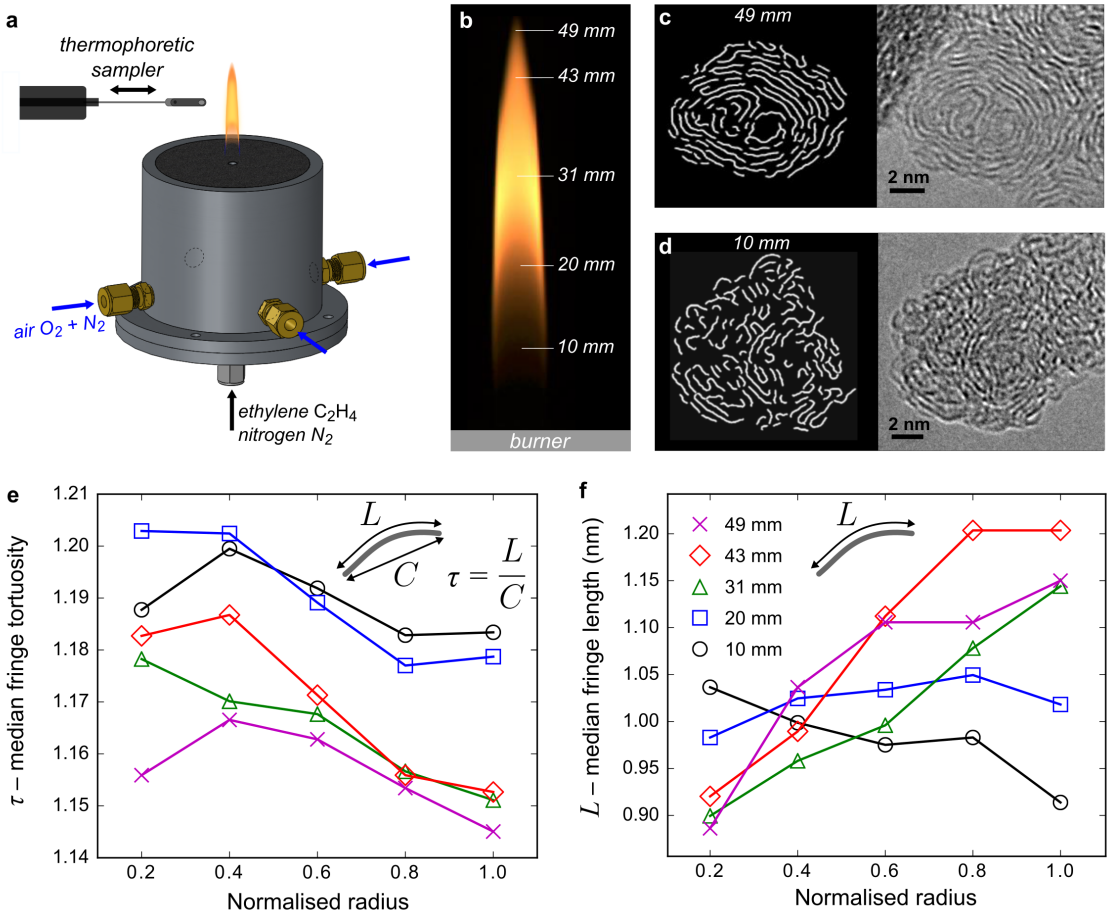

Figure 2: ***HRTEM analysis of carbon nanoparticulates:*** ***a****, Schematic of the co-flow diffusion flame used and the rapid solenoid injector, and* ***b****, sampling positions.* ***c-d****, Skeletonised and unprocessed HRTEM images of primary carbon nanoparticulates for 10 and 49 mm heights above the burner (particles are not shown to scale but have radii of 9.5–10 and 8.5–10.2 nm; unprocessed images are also shown).* ***e-f****, Fringe median length and tortuosity as a function of the radial distance normalised to the size of the primary particles for various heights above the burner (standard errors* ± 0.01 *for* τ*, and* ± 0.03 *nm for* L*).*

from the late stages of the flame have considerably flatter and longer fringes, indicating a carbonisation process leading to removal of embedded pentagonal rings.

The polarity of curved PAHs in the carbon particulates at 10 mm above the burner can be estimated based on the median fringe length ($L \sim 1$ nm) and tortuosity ($\tau \sim 1.2$) suggested from HRTEM image analysis of early carbon nanoparticles, which correspond to the curved PAH containing two pentagons (Figure 3b). We calculated a dipole moment of 5.32 D for this species using the methodology developed previously [28]. Figure 3d shows the electrostatic potential perpendicular to the aromatic plane of the PAH and reveals significant charge polarisation due to the flexoelectric effect. The electrostatic potential indicates strong binding sites for cations on the convex and concave surfaces of the

aromatic plane.

For chemi-ions and curved PAHs to interact at flame temperatures where carbon particulates form (1300-1500 K) large intermolecular interaction energies are required to stabilise molecular clusters. For planar PAHs with 13–19 rings we have previously determined the dissociation energy required to stabilise clusters at these temperatures at $E_\mathrm{d} = -140$–180 kJ/mol (shown as the green range (i) in Figure 3e) [42]. The chemi-ion $C_3H_3^+$ is the most abundant cation in sooting flames and is a likely candidate for a nucleation centre in a nucleation mechanism [16]. Chen and Wang recently used coupled cluster calculations to analyse the binding of $C_3H_3^+$ with planar PAHs [4]. They found that the stable configurations occurred when the cation bonded around the rim of the planar PAH, saturating for PAHs containing more than five aromatic rings at binding energies of -60–112 kJ/mol (shown as the grey range (ii) in Figure 3e), which is insufficient to stabilise these complexes under flame-relevant temperatures.

We calculated the binding energies between the curved PAH we identified as a likely component in carbon particulates (Figure 3b) and $C_3H_3^+$ using hybrid density functional theory with a dispersion correction [15]. This level of theory has previously been found to accurately predict binding energies of cation-benzene complexes and of dimers of the curved PAH corannulene (within ± 4 kJ/mol) compared to benchmark coupled cluster calculations [19, 32]. We confirmed that this methodology also correctly reproduces the dipole moment of corannulene compared with our previous calculations [28], indicating that the electrostatic and dispersion interactions are each being described with satisfactory accuracy. Figure 3f-h shows the geometries of the three most stable binding sites of $C_3H_3^+$. A similar binding site to planar PAHs was found around the rim of the curved PAH (Figure 3g), however, unlike the planar geometries, binding on the centre of the aromatic faces was stronger than on the rim. The binding site with the highest binding energy was found for the concave surface (Figure 3h), where the cupped geometry enhanced the dispersion interactions and the negative electric potential due to the π-orbitals. The binding site at the centre of the convex surface (Figure 3f) is dominated by the flexoelectric dipole-ion interaction: a classical electrostatic charge-dipole interaction at the intermolecular distance of 3 Å gives a similar binding energy of -171 kJ/mol using the dipole moment 5.32 D calculated earlier. Figure 3i shows the curved PAH homodimer with an energy of $E_\mathrm{d} = -150$ kJ/mol, which is comparable to a similar sized planar PAH of -144 kJ/mol (interpolated from the Totton et al. benchmark calculations based on the number of carbon atoms [42]) indicating similar clustering behaviour to planar PAHs is expected for homogeneous nucleation of this curved PAH.

For larger clusters of the curved PAH stabilised by an ion, geometry optimisations were performed from different possible starting geometries to ensure stable energy minima were found for the dimer, trimer and tetramer (with the binding energies E_b shown in Figure 3j-l as grey bars). Unlike planar PAHs, which see a significant decrease in binding energy with a chemi-ion for subsequent additions after the dimer, the binding energies of clusters of curved PAHs stabilised with a chemi-ion continues to increase linearly towards that of the tetramer [4]. The stacking geometry of the curved PAH is stabilised by the dispersion and dipole-dipole interactions being further strengthened by the electrostatic and inductive interactions with the chemi-ion. We also calculated the dissociation energies E_d as the energy required to remove a monomer from the complex (shown in Figure 3j-l

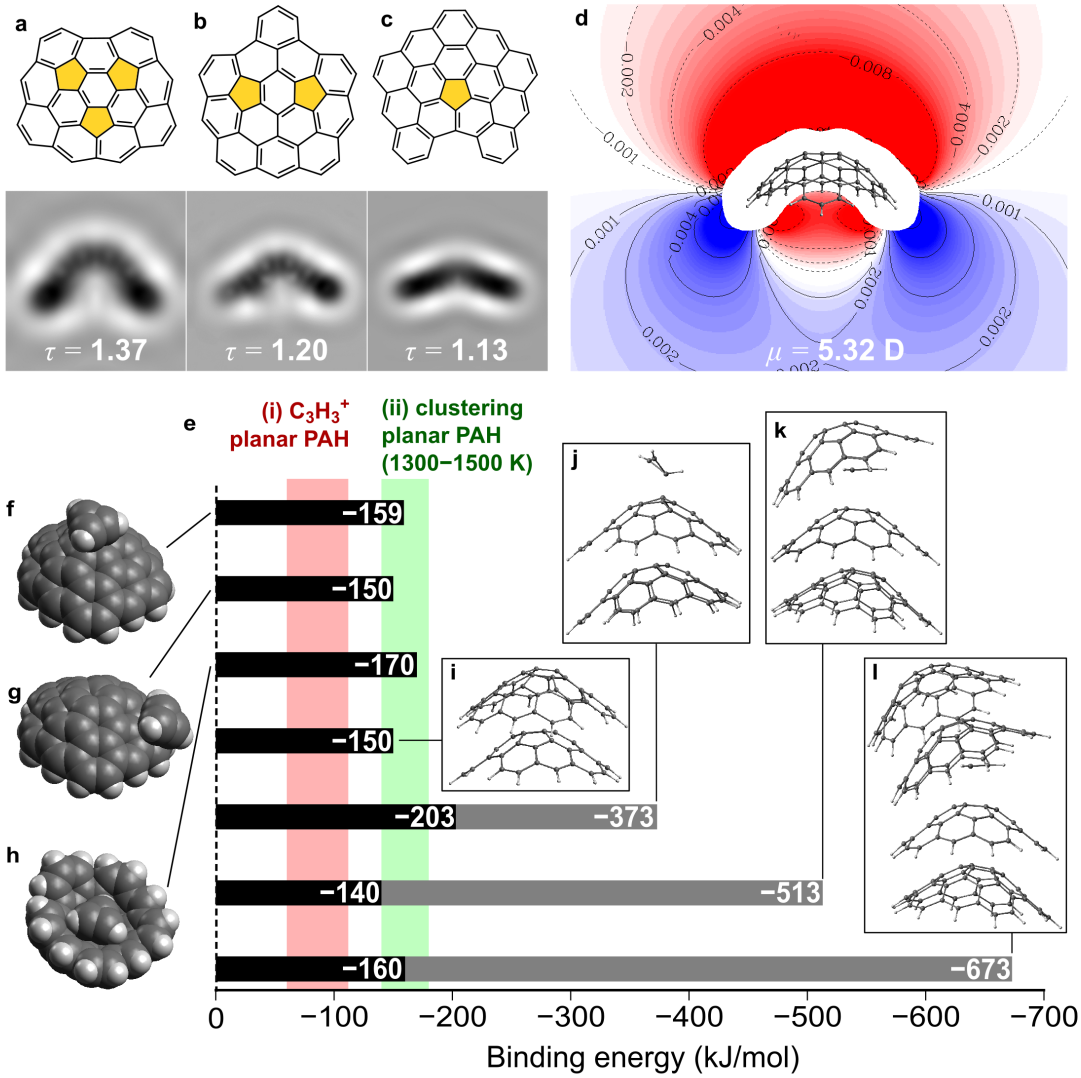

Figure 3: ***Simulated HRTEM images, flexoelectric electric potential and DFT-D binding energies:*** ***a-c,*** *Curved aromatics with three, two and one pentagons, respectively, with simulated HRTEM images (with their corresponding calculated tortuosity value).* ***d,*** *Electrostatic potential perpendicular to the aromatic plane for the curved PAH with two pentagons (isovalues of the potential are shown in a.u.).* ***e,*** *Dissociation energies for the cation-curved PAH complexes (black bar). The red region (i) shows the range of binding energies calculated previously for planar PAHs binding to* $C_3H_3^+$ *[4]; the green (ii) shows the region of binding energies that were found to allow large planar PAHs to cluster at 1300–1500 K [42].* ***f-h,*** *Optimised geometries of binding sites for the chemi-ion* $C_3H_3^+$ *on the curved PAH* ***b****.* ***i,*** *Geometries of the dimer of the curved PAH* ***b****.* ***h-j,*** *Cluster geometries for the dimer, trimer and tetramer with the chemi-ion* $C_3H_3^+$ *(grey bar shows complexes total binding energies).*

as black bars). All of the dissociation energies calculated between the chemi-ion $C_3H_3^+$ with a representative polar curved PAH are found to be in the range to allow planar PAH to cluster at flame temperatures suggesting these interactions play a role in stabilising carbon particulate nuclei.

In order to fully understand the role of chemi-ions in nuclei formation further work is needed. Firstly, more experimental work is required to determine the amounts of polar and non-polar aromatic PAHs present in the gas phase where nucleation is taking place. Secondly, computational work is required to determine whether these collections of curved PAHs form nuclei around chemi-ions at flame temperatures and how this mechanism competes with homogeneous nucleation or a chemical inception mechanism under different combustion conditions. However, we can consider some potential applications of such an ionic mechanism. It could provide a new route to reduce carbon particulate pollution. Additives could be incorporated into fuels or engine operating conditions modified to reduce the curvature integrated into aromatics in flames in order to reduce interaction energies with cations and thereby reduce production of particulates. This understanding could also improve flame synthesis of nanoparticles such as fullerenes or graphene by inhibiting the pathways to particulate formation. While these details and applications remain to be explored, this work provides for the first time evidence of the significant role of the curved PAHs and the polar PAH-ion interaction in carbon particulate formation in flames.

4 Conclusions

To conclude, we present strong evidence of enrichment of the nascent carbon nanoparticles in curved polar PAH molecules. If 25% of the PAHs found in the gas phase contain pentagonal rings [9]and that in the earliest carbon nanoparticles we could sample the content of curved molecular fragments is at least 62.5%, as it follows from the fringe analysis of the HRTEM images, then curved species appear to be enriched in early carbon nanoparticles. The result can be explained with nucleation of curved PAHs on ions in the flame; the likelihood of this hypothesis is demonstrated by the high binding energies of the flame ion $C_3H_3^+$ to a representative curved PAH, and with the high stability of larger complexes of several curved polar PAHs and the ion, as computed from electronic structure calculations.

Acknowledgements

This project is supported by the National Research Foundation (NRF), Prime Minister's Office, Singapore under its Campus for Research Excellence and Technological Enterprise (CREATE) programme. This work used the ARCHER UK National Supercomputing Service (http://www.archer.ac.uk).

5 Appendix

Co-flow burner and soot sampling

Soot was produced on a co-flow burner which has previously been described [41]. The burner consists of a central fuel tube with an inner diameter of 3/16" and outer diameter of 11/64" and a concentric air co-flow tube with an inner diameter of 2.9". The fuel velocity at the burner surface had a parabolic profile and the air co-flow was plug flow produced by a honeycomb on top, both with an average velocity of 35 cm/s. The fuel, nitrogen and air flow rates are 134.7 ml/min (±1%), 91.2 ml/min (±1%) and 89.1 l/min (±2%). The visible flame height was approximately 50 mm from the fuel tube exit. A diagram of the burner with labelled components is shown in Figure S1.

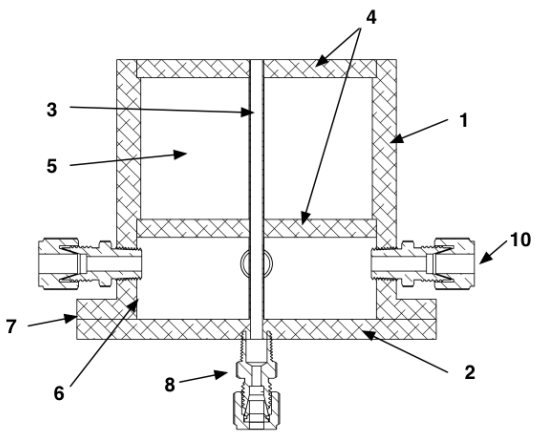

Figure S1: *Cross-section schematic of the Yale burner [41] with components labelled: 1) housing, 2) bottom plate, 3) fuel tube 4.0 mm inner diameter, 4) stainless steel honeycomb, 5) glass beads, 6) screen, 7) O-ring, 8) fuel tube support fitting and 10) air connection fitting.*

The methodology for the sampling of soot in the flame has been previously detailed [2]. A probe was rapidly inserted into the flame using two linear solenoids connected to each other such that one pushes forwards and the other backwards. The system was controlled by a programmable logic controller (PLC) that triggered each solenoid with a lag time in between, which could be adjusted to change the exposure of the sampler in the flame. The sampler was mounted on one of the solenoids and consisted of two metallic sheets used to hold the TEM grid. The soot was then thermophoretically driven towards a carbon-coated copper grid used in electron microscopy [8]. A high-speed camera was employed to time the exposure of the grid in the flame to 30–46 ms.

High resolution transmission electron microscopy

High resolution transmission electron microscopy (HRTEM) images were collected on a JEOL 2100F with an operating voltage of 200 kV and point resolution of 0.19 nm.

Primary soot particles ranging from 10–30 nm were imaged in vacuum with a total of 130 images collected and 209 primary particles analysed. All images were collected at the same magnification to allow for straightforward comparison. Images were collected on the grids before placing them into the flame to make sure the structures observed were originating from the flame. For sampling along the centre line below the yellow soot emission, the injector must pass through the wings, which form soot earlier than the centreline does. Images of soot sampled from the same height as the wings were compared with those taken from the centreline. Many small (<10 nm) soot particles were found in the centreline sampled images which were not observed in the wings and these were the soot particles taken as originating from the centreline and not from the wings. These small soot particles early in the flame along the centreline have also been experimentally observed using synchrotron radiation [6].

Fringe-lattice analysis

The TEM images were processed using in-house software written in Matlab and detailed in the previous work by Botero et al. [2]. Figure S2 shows a histogram of fringe lengths calculated from all of the soot particles imaged. A significant positive skew can be observed for the distribution. In order to comment on the fringe morphology, the median was chosen as a metric that is less sensitive to the skew of the distribution, a feature that can be problematic when comparing the mean, which is sensitive to outliers.

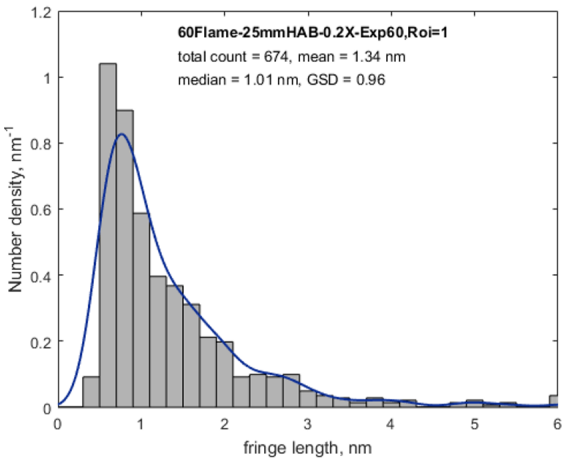

Figure S2: *Fringe length distribution for all fringes analysed.*

The region of interest was chosen so that there were no overlapping regions from other primary particles, allowing the fringes to be clearly resolved. The software was extended to allow for the properties of the fringes to be calculated as a function of radius from the centre of the particle. The primary particles constitute almost spherical structure. The centre was determined visually by the operator and the radius of the sphere was chosen so that all of the fringes were inside the region of interest. The fringes were then divided into five regions depending on the normalised radial distance from the centre (0.0–0.2, 0.2–0.4, 0.4–0.6, 0.6–0.8, 0.8–1.0) and the fringe length and tortuosity were calculated for each region at different heights above the burner. The total number of fringes analysed

was 28700. Other partitioning schemes were attempted, such as equal area shells, but similar trends were found and we found the radial partitioning was the most straightforward procedure. The large number of fringes and particles analysed allowed the tortuosity and fringe length to be determined at each different heights and radii with a standard error of $\tau - \pm 0.01$ and $L - \pm 0.03$ nm, respectively. While the whole of each particle could be imaged, the resolution in the outermost radial shell is better and the respective distributions are more accurate. Quantifying this accuracy the fringe length and tortuosity standard errors at the perimeter to the centre were found to slightly increase from ± 0.02 to ± 0.04 and ± 0.01 to ± 0.02, respectively. This increase was still minimal compared with the measured values with percentage errors increasing from 1% at the perimeter to 3% and 2% for the centre most shell for fringe length and tortuosity, respectively.

Simulated electron microscopy images

In order to interpret the fringes measured using HRTEM, a selection of aromatic molecules were chosen and their electron micrographs simulated using multislice methods. These images were then analysed using our fringe analysis software. We have previously used this methodology on planar molecules to determine fringe lengths [2]. The multislice software detailed in the book *Advanced computing in electron microscopy* by Kirkland [21] was used to simulate the propagation and scattering of electrons through the molecular structure.

Aromatics with fringe lengths of $\sim$1 nm were chosen. Figure S3 shows the molecular geometry, simulated fringe and processed skeletonised fringes with their calculated tortuosity values. Figure S3a-c shows three different curved aromatic molecules containing one, two and three pentagons. The structures are seen to produce continuously curved fringes with tortuosity values of 1.13–1.37. Figure S3d-e shows crosslinked planar pyrene and planar circumpyrene. The angle of the pyrene dimer was changed to produce the most well-resolved fringes. This was also the structure with the greatest tortuosity value of 1.14, compared with the pentagon containing aromatic molecules – a similar value to that of a curved PAH with one pentagon integrated.

Electronic structure calculations

The hybrid density functional theory with an empirical dispersion correction, B97D, was used to determine the geometry-optimised structures for a variety of clusters [15]. The geometry optimised at the B97D/6-311G(d,p) level of theory was followed by a single point calculation at the B97D/cc-pVTZ level of the dipole moment; for corannulene, the value 2.08 D has been calculated, compared with the experimental value of 2.07 D calculated using rotational spectroscopy [26]. The binding energy of dimers of corannulene or sumanene was found to be within 2% of the benchmark calculations at the CCSD(T) level of theory of these energies [19]. B97D was also found to perform well (to within 1.3 kJ/mol) compared with benchmark calculation of Na^+-benzene binding energy at a similar level of theory [32]. Basis set superposition errors for the dimer were calculated to be $<$2 kJ/mol at the B97D/cc-pVTZ level of theory, small enough to not include in

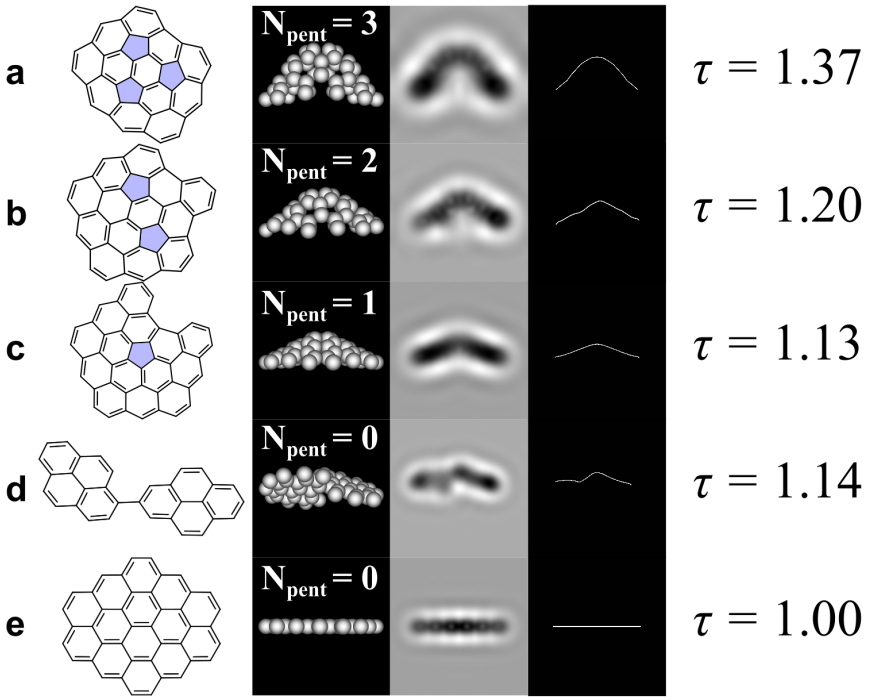

Figure S3: *Simulated TEM images of PAHs ∼1 nm in length, curved PAH with three a), two b) and one pentagon c), pyrene dimer d) and circumpyrene e). Columns from the left show the 2D molecular structure, 3D orientations, simulated TEM images, skeletonised fringes and tortuosity values.*

the final energies. A variety of different starting configurations were used and frequency calculations were performed on all of the clusters to ensure that a suitable minima was found for each cluster.

References

[1] M. L. Botero, E. M. Adkins, S. González-Calera, H. Miller, and M. Kraft. PAH structure analysis of soot in a non-premixed flame using high-resolution transmission electron microscopy and optical band gap analysis. *Combustion and Flame*, 164:250–258, 2016. doi:10.1016/j.combustflame.2015.11.022.

[2] M. L. Botero, D. Chen, S. González-Calera, D. Jefferson, and M. Kraft. HRTEM evaluation of soot particles produced by the non-premixed combustion of liquid fuels. *Carbon*, 96:459–473, 2016. doi:10.1016/j.carbon.2015.09.077.

[3] H. F. Calcote, D. B. Olson, and D. G. Keil. Are ions important in soot formation? *Energy & Fuels*, 2(4):494–504, 1988. doi:10.1021/ef00010a016.

[4] D. Chen and H. Wang. Cation-π interactions between flame chemi-ions and aromatic compounds. *Energy & Fuels*, 31(3):2345–2352, 2017. doi:10.1021/acs.energyfuels.6b02354.

[5] S. L. Chung and N. L. Lai. Suppression of soot by metal additives during the combustion of polystyrene. *Journal of the Air and Waste Management Association*, 42 (8):1082–1088, 1992. doi:10.1080/10473289.1992.10467056.

[6] S. Di Stasio, J. B. a. Mitchell, J. L. Legarrec, L. Biennier, and M. Wulff. Synchrotron SAXS in situ identification of three different size modes for soot nanoparticles in a diffusion flame. *Carbon*, 44(7):1267–1279, 2006. doi:10.1016/j.carbon.2005.10.042.

[7] S. Di Stasio, J. L. Legarrec, and J. B. Mitchell. Synchrotron radiation studies of additives in combustion, II: Soot agglomerate microstructure change by alkali and alkaline-earth metal addition to a partially premixed flame. *Energy and Fuels*, 25 (3):916–925, 2011. doi:10.1021/ef1012209.

[8] R. A. Dobbins and C. M. Megaridis. Morphology of flame-generated soot as determined by thermophoretic sampling. *Langmuir*, 3(2):254–259, 1987. doi:10.1021/la00074a019.

[9] A. Fialkov. Investigations on ions in flames. *Progress in Energy and Combustion Science*, 23:399–528, 1997. doi:10.1016/S0360-1285(97)00016-6.

[10] M. Frenklach. Reaction mechanism of soot formation in flames. *Physical Chemistry Chemical Physics*, 4(11):2028–2037, 2002. doi:10.1039/b110045a.

[11] M. Frenklach and L. B. Ebert. Comment on the proposed role of spheroidal carbon clusters in soot formation. *The Journal of Physical Chemistry*, 92(2):561–563, 1988. doi:10.1021/j100313a061.

[12] M. Frenklach, M. Ramachandra, and R. Matula. Soot formation in shock-tube oxidation of hydrocarbons. *Symposium (International) on Combustion*, 20(1):871 – 878,

1985. doi:https://doi.org/10.1016/S0082-0784(85)80576-2. Twentieth Symposium (International) on Combustion.

[13] P. Gerhardt, S. LÃűffler, and K. Homann. Polyhedral carbon ions in hydrocarbon flames. *Chemical Physics Letters*, 137(4):306 – 310, 1987. ISSN 0009-2614. doi:https://doi.org/10.1016/0009-2614(87)80889-8.

[14] I. Glassman. Soot formation in combustion processes. *Symposium (International) on Combustion*, 22(1):295–311, 1989. doi:10.1016/S0082-0784(89)80036-0.

[15] S. Grimme. Semiempirical GGA-type density functional constructed with a long-range dispersion correction. *Journal of Computational Chemistry*, 27(15):1787–1799, nov 2006. doi:10.1002/jcc.20495.

[16] A. N. Hayhurst and H. R. N. Jones. Ions and soot in flames. *Journal of the Chemical Society, Faraday Transactions 2*, 83(1):1, 1987. doi:10.1039/f29878300001.

[17] B. S. Haynes and H. G. Wagner. Soot formation. *Progress in Energy and Combustion Science*, 7(4):229–273, 1981. doi:10.1016/0360-1285(81)90001-0.

[18] J. B. Howard and W. J. Kausch. Soot control by fuel additives. *Progress in Energy and Combustion Science*, 6(3):263–276, 1980. doi:10.1016/0360-1285(80)90018-0.

[19] T. Janowski, P. Pulay, A. A. Sasith Karunarathna, A. Sygula, and S. Saebø. Convex-concave stacking of curved conjugated networks: Benchmark calculations on the corannulene dimer. *Chemical Physics Letters*, 512(4-6):155–160, 2011. doi:10.1016/j.cplett.2011.07.030.

[20] D. Kashchiev. *Nucleation*. Butterworth-Heinemann, 2000.

[21] E. J. Kirkland. *Advanced computing in electron microscopy*. Springer Science & Business Media, 2010.

[22] A. L. Lafleur, J. B. Howard, J. A. Marr, and T. Yadav. Proposed fullerene precursor corannulene identified in flames both in the presence and absence of fullerene production. *The Journal of Physical Chemistry*, 97(51):13539–13543, 1993. doi:10.1021/j100153a020.

[23] P. J. Landrigan, R. Fuller, N. J. R. Acosta, O. Adeyi, R. Arnold, N. N. Basu, A. B. Baldé, R. Bertollini, S. Bose-O'Reilly, J. I. Boufford, P. N. Breysse, T. Chiles, C. Mahidol, A. M. Coll-Seck, M. L. Cropper, J. Fobil, V. Fuster, M. Greenstone, A. Haines, D. Hanrahan, D. Hunter, M. Khare, A. Krupnick, B. Lanphear, B. Lohani, K. Martin, K. V. Mathiasen, M. A. McTeer, C. J. L. Murray, J. D. Ndahimananjara, F. Perera, J. Potočnik, A. S. Preker, J. Ramesh, J. Rockström, C. Salinas, L. D. Samson, K. Sandilya, P. D. Sly, K. R. Smith, A. Steiner, R. B. Stewart, W. A. Suk, O. C. P. van Schayck, G. N. Yadama, K. Yumkella, and M. Zhong. The lancet commission on pollution and health. *The Lancet*, 2017. doi:10.1016/S0140-6736(17)32345-0.

[24] J. Lawton and F. Weinberg. *Electrical aspects of combustion*. Clarendon P., 1969.

[25] J. Lighty, V. Romano, A. Sarofim, H. Bockhorn, A. D'Anna, A. Sarofim, and H. Wang. *Combustion generated fine carbonaceous particles*. KIT Scientific Publishing, 2009.

[26] F. J. Lovas, R. J. McMahon, J. U. Grabow, M. Schnell, J. Mack, L. T. Scott, and R. L. Kuczkowski. Interstellar chemistry: A strategy for detecting polycyclic aromatic hydrocarbons in space. *Journal of the American Chemical Society*, 127(12):4345–4349, 2005. doi:10.1021/ja0426239.

[27] E. R. Magaril and R. Z. Magaril. *Engine fuels*. KDU, Moscow, 2008.

[28] J. W. Martin, R. I. Slavchov, E. K. Y. Yapp, J. Akroyd, S. Mosbach, and M. Kraft. The polarization of polycyclic aromatic hydrocarbons curved by pentagon incorporation: the role of the flexoelectric dipole. *The Journal of Physical Chemistry C*, 121 (48):27154–27163, 2017. doi:10.1021/acs.jpcc.7b09044.

[29] J. W. Martin, K. L. Bowal, A. Menon, R. I. Slavchov, J. Akroyd, S. Mosbach, and M. Kraft. Polar curved polycyclic aromatic hydrocarbons in soot formation. *Proceedings of the Combustion Institute*, In Press, Corrected Proof, 2018. doi:10.1016/j.proci.2018.05.046.

[30] P. J. Mayo and F. J. Weinberg. On the size, charge and number-rate of formation of carbon particles in flames subjected to electric fields. *Proceedings of the Royal Society A: Mathematical, Physical and Engineering Sciences*, 319(1538):351–371, 1970. doi:10.1098/rspa.1970.0183.

[31] J. R. McConnell, R. Edwards, G. L. Kok, M. G. Flanner, C. S. Zender, E. S. Saltzman, J. R. Banta, D. R. Pasteris, M. M. Carter, and J. D. W. Kahl. 20th-Century Industrial Black Carbon Emissions Altered Arctic Climate Forcing. *Science*, 317 (5843):1381–1384, 2007. doi:10.1126/science.1144856.

[32] A. R. Neves, P. A. Fernandes, and M. J. Ramos. The accuracy of density functional theory in the description of cation-π and π-hydrogen bond interactions. *Journal of Chemical Theory and Computation*, 7(7):2059–2067, 2011. doi:10.1021/ct2001667.

[33] A. A. Onischuk, S. Di Stasio, V. V. Karasev, A. M. Baklanov, G. A. Makhov, A. L. Vlasenko, A. R. Sadykova, A. V. Shipovalov, and V. N. Panfilov. Evolution of structure and charge of soot aggregates during and after formation in a propane/air diffusion flame. *Journal of Aerosol Science*, 34(4):383–403, 2003. doi:10.1016/S0021-8502(02)00215-X.

[34] D. G. Park, B. C. Choi, M. S. Cha, and S. H. Chung. Soot reduction under DC electric fields in counterflow non-premixed laminar ethylene flames. *Combustion Science and Technology*, 186(4-5):644–656, 2014. doi:10.1080/00102202.2014.883794.

[35] E. R. Place and F. J. Weinberg. Electrical control of flame carbon. *Proceedings of the Royal Society A: Mathematical, Physical and Engineering Sciences*, 289(1417): 192–205, jan 1966. doi:10.1098/rspa.1966.0006.

[36] H. Richter, A. J. Labrocca, W. J. Grieco, K. Taghizadeh, A. L. Lafleur, and J. B. Howard. Generation of higher fullerenes in flames. *Journal of Physical Chemistry B*, 101(9):1556–1560, 1997. doi:10.1021/jp962928c.

[37] Y. Rong, X. Hou, Y. Hu, A. Mei, L. Liu, P. Wang, and H. Han. Synergy of ammonium chloride and moisture on perovskite crystallization for efficient printable mesoscopic solar cells. *Nature Communications*, 8:14555, feb 2017. doi:10.1038/ncomms14555.

[38] M. Saito, T. Arai, and M. Arai. Control of soot emitted from acetylene diffusion flames by applying an electric field. *Combustion and Flame*, 119(3):356–366, 1999. doi:10.1016/S0010-2180(99)00065-6.

[39] S. L. Shostak, W. L. Ebenstein, and J. S. Muenter. The dipole moment of water. I. Dipole moments and hyperfine properties of H_2O and HDO in the ground and excited vibrational states. *The Journal of Chemical Physics*, 94(9):5875, 1991. doi:10.1063/1.460471.

[40] J. Simonsson, N. E. Olofsson, H. Bladh, M. Sanati, and P. E. Bengtsson. Influence of potassium and iron chloride on the early stages of soot formation studied using imaging LII/ELS and TEM techniques. *Proceedings of the Combustion Institute*, 36 (1):853–860, 2017. doi:10.1016/j.proci.2016.07.003.

[41] M. D. Smooke, C. S. McEnally, L. D. Pfefferle, R. J. Hall, and M. B. Colket. Computational and experimental study of soot formation in a coflow, laminar diffusion flame. *Combustion and Flame*, 117(1):117–139, 1999. doi:10.1016/S0010-2180(98)00096-0.

[42] T. S. Totton, A. J. Misquitta, and M. Kraft. A quantitative study of the clustering of polycyclic aromatic hydrocarbons at high temperatures. *Physical chemistry chemical physics*, 14(12):4081–94, 2012. doi:10.1039/c2cp23008a.

[43] C. Wang, T. Huddle, C. H. Huang, W. Zhu, R. L. Vander Wal, E. H. Lester, and J. P. Mathews. Improved quantification of curvature in high-resolution transmission electron microscopy lattice fringe micrographs of soots. *Carbon*, 117:174–181, 2017. doi:10.1016/j.carbon.2017.02.059.

[44] H. Wang. Formation of nascent soot and other condensed-phase materials in flames. *Proceedings of the Combustion Institute*, 33(1):41–67, 2011. doi:10.1016/j.proci.2010.09.009.

[45] Y. Wang, J. Kangasluoma, M. Attoui, J. Fang, H. Junninen, M. Kulmala, T. Petäjä, and P. Biswas. The high charge fraction of flame-generated particles in the size range below 3 nm measured by enhanced particle detectors. *Combustion and Flame*, 176: 72–80, 2017. doi:10.1016/j.combustflame.2016.10.003.

[46] R. Whitesides and M. Frenklach. Detailed kinetic Monte Carlo simulations of graphene-edge growth. *The Journal of Physical Chemistry. A*, 114(2):689–703, 2010. doi:10.1021/jp906541a.

[47] X. Z. Wu, Y. R. Yao, M. M. Chen, H. R. Tian, J. Xiao, Y. Y. Xu, M. S. Lin, L. Abella, C. B. Tian, C.-L. Gao, Q. Zhang, S. Y. Xie, R. B. Huang, and L. S. Zheng. Formation of curvature subunit of carbon in combustion. *Journal of the American Chemical Society*, 138(30):9629–9633, 2016. doi:10.1021/jacs.6b04898.

[48] E. K. Yapp, C. G. Wells, J. Akroyd, S. Mosbach, R. Xu, and M. Kraft. Modelling PAH curvature in laminar premixed flames using a detailed population balance model. *Combustion and Flame*, 176:172–180, 2017. doi:10.1016/j.combustflame.2016.10.004.

[49] A. V. Zabula, A. S. Filatov, S. N. Spisak, A. Y. Rogachev, and M. A. Petrukhina. A main group metal sandwich: five lithium cations jammed between two corannulene tetraanion decks. *Science*, 333(6045):1008–1011, 2011. doi:10.1126/science.1208686.